CHEMISTRY OF MATERIALS

pubs.acs.org/cm

Article

Reducing the Thermal Effects during Coating of Superconducting Radio-Frequency Cavities: A Case Study for Atomic Layer Deposition of Alumina with a Combined Numerical and Experimental Approach

Getnet Kacha Deyu,* Trupen Parikh, Marc Wenskat, Isabel González Díaz-Palacio, Robert H. Blick, Robert Zierold, and Wolfgang Hillert

Cite This: *Chem. Mater.* 2024, 36, 2846−2856

Read Online

ACCESS | Metrics & More | Article Recommendations | Supporting Information

ABSTRACT: Coating the inner surface of superconducting radio frequency (SRF) cavities is one of the strategies to push ultimate limits in next generation accelerators. One of the potential coating techniques for such intricate and large volume structures is atomic layer deposition (ALD), as it offers full and uniform layer coverage. In order to predict the process parameters for coating SRF cavities on the large substrates with ALD, we simulate the ALD of alumina (Al_2O_3) on the ANSYS Fluent 19.1 commercial package by solving vapor transport and chemistry equations. The computational domain in the numerical model is based on the homemade ALD setup for thin film sample chamber and a 1.3 GHz Tesla-shaped niobium cavity. Trimethlyaluminum (TMA) and water (H_2O) were used as precursors. In the simulation process for the cavity, two steps were carried out: first, the simulation of precursor distribution, followed by the simulation of surface reactions. The simulations show that saturation is achieved with precursor pulses of only 50 ms after 1.05 s for TMA and 750 ms for H_2O, obviating the necessity for prolonged exposure times. Furthermore, the resulting predicted growth per cycle of these process times of ≈1.22 Å for Al_2O_3 was experimentally validated, affirming the credibility of our simulations. Experimental findings also showcased a remarkable 66.2% reduction in process time while upholding film homogeneity and quality. Our approach presented here carries profound importance, particularly for coating intricate and large volume structures, like SRF cavities, and provides another approach to minimize time- and resource-intensive parameter scans.

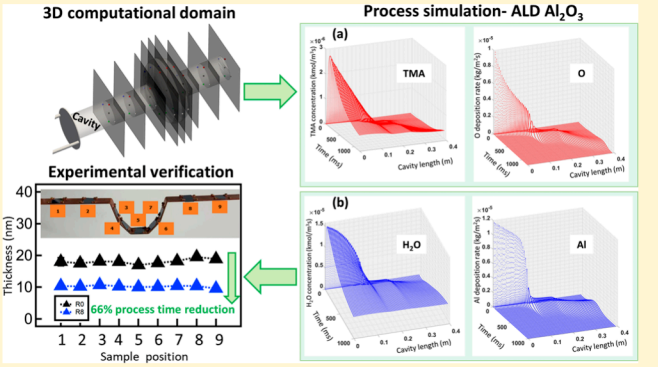

1. INTRODUCTION

Superconducting radio frequency (SRF) systems based on bulk niobium (Nb) have been the backbone of particle accelerators, offering exceptional performance and reliability. Achieving the remarkable performance of bulk Nb SRF cavities has been the result of over five decades of intensive research aimed at optimizing the material.[1] Recent improvements in SRF technology have introduced a range of innovative surface treatments. These treatments have enabled Nb cavities to achieve quality factors (Q_0) higher than those of previous records, all while maintaining their performance with increasing gradients. These advancements encompass methods such as nitrogen doping and infusion as well as mid-T baking.[2−4] To move beyond the intrinsic limitations of niobium, only few concepts have been suggested including superconductor−insulator-superconductor (SIS) multilayer structures.[5−7] Coating the inner surface of Nb cavities with thin films or multilayers of superconductors, such as NbN or NbTiN, and insulators, such as Al_2O_3 or AlN, holds the potential to create advanced composite accelerator cavities. These coated cavities are anticipated to outperform traditional Nb cavities, achieving lower RF losses and higher accelerating gradients, potentially exceeding 100 MV/m.[8] It is crucial to highlight that gurovich's model[8] fails to provide an accurate representation of SRF cavities, leading to a conclusion of an arbitrary rise in the critical field for such cavities. Subsequent investigations[9,10] have emphasized the significance of incorporating substrate considerations into the model for precise predictions regarding the critical field increase.

Atomic layer deposition (ALD) is a vapor-phase deposition technique known for its ability to synthesize ultrathin films. These films are typically grown submonolayer by submonolayer, achieved through the repeated execution of two distinct half-cycles.[11−16] The presence of steric and electrostatic

Received: December 13, 2023
Revised: February 16, 2024
Accepted: February 20, 2024
Published: March 5, 2024

hindrance from ligands, specifically those associated with the chemisorbed first reactant, poses a challenge by shielding portions of the surface, limiting accessibility for the second reactant. Consequently, the growth per cycle (GPC) in ALD, especially when employing compound reactants, as examined in this study, is expected to be significantly less than that of a monolayer. Experimental GPC values exhibit variability within the range of 15−30% of a monolayer, contingent upon the growth temperature.[12,17] ALD technology offers the possibility to prepare thin films of high quality materials with no line-of-sight deposition, precise thickness control, high uniformity, and excellent conformality. ALD is particularly well suited for coating complex structures with high aspect ratios and large substrate areas, making it an excellent choice for coating structures such as SRF cavities.

The deposition of Al_2O_3 using trimethylaluminum (TMA) and water as precursors is among the most extensively studied ALD processes on different substrates such as metals, metal oxides, and semiconductors.[12,18,19] In the TMA/water process, the reactive surface sites are OH and $Al(CH_3)$ for TMA and water, respectively. Al_2O_3 films deposited by ALD are known for their density, stability, and exceptional dielectric passivation properties, especially on metallic surfaces.[20,21] These qualities make Al_2O_3 a promising material to be used as an insulating layer which has been shown to preserve Nb superconductivity.[22,23]

There are handful studies reported on the experimental work of SRF cavities coated with ALD Al_2O_3.[23−27] Proslier et al. utilized thermal ALD to coat cavities with a thin layer of Al_2O_3 and Al_2O_3/Nb_2O_5 bilayers at ≥200 °C. Their results indicated a significant increase in field emission and multipacting, limiting several cavities to around 20 MV/m and causing an increase in surface resistance.[25] Subsequent studies using the same parameters but in a new setup experienced similar issues with cavity performance.[26] While a cavity with an Al_2O_3/Nb_2O_5 bilayer coating achieved an accelerating field of up to 33 MV/m, it also exhibited increased surface resistance.[27] In another study, Eremeev et al. coated a cavity with Al_2O_3 using thermal ALD within a temperature range of 100−150 °C.[24] A cloudy white discoloration on some regions of the cavity surface was observed after deposition, which results in a significant deterioration of the cavity performance.[24] This can be attributed to the nonuniform coating, possibly due to unoptimized process parameters and temperature variations within a cavity volume. In contrast, our own research leads to a successful low-temperature coating of 1.3 GHz Tesla-shaped SRF cavities at 120 °C with insulating Al_2O_3 using thermal ALD.[23] The coating process involved pulsing TMA for 500 ms, followed by an exposure time of 60 s, and purging for 120 s during the first half cycle. In the second half cycle, water was pulsed for 500 ms, followed by an exposure time of 60 s and purging for 120 s. Remarkably, this coating did not compromise the cavity's maximum achievable accelerating field, which exceeded 40 MV/m.[23] Moreover, an improvement in the surface resistance surpassing 30 MV/m was observed. This improvement is attributed to enhanced oxygen diffusion facilitated by the deposition process. From these studies, the duration for individual steps of pulse, exposure, and purge times of the ALD process is only reported by Wenskat et al.[23]

The thermal effects in the coating of SRF cavities are crucial for budgeting, as the temperature during the process significantly influences adhesion, crystallinity, and overall coating quality. Thus, a precise control of the deposition temperature is imperative in order to attain the desired film properties. The thermal environment during the coating process is instrumental in shaping both the nucleation of the thin film and the adhesion of the coating to the cavity surface, emphasizing the importance of maintaining a proper temperature control for robust adherence and a uniform nucleation process. This understanding and control of thermal effects have become paramount for the optimization of the coating process. In essence, the diligent management of temperature during the coating of SRF cavities is indispensable for achieving superior-quality, uniform, and well-adhered thin film coatings. Furthermore, care must be given while selecting coating temperature and time in a way to minimize the impact of temperature on dissolution of native oxides and other diffusion processes which may alter the cavity performance.[28−33] Notably, high-temperature depositions of different sputtering processes are necessary for depositing superconducting films on Nb or Cu substrates, highlighting the need to tailor temperature to specific materials and deposition techniques.[5,6]

Given the high cost of superconducting cavities, the time and resources required for RF tests in cryogenic environments and the use of surface resets containing various harmful acids, it is crucial to minimize the number of cavity coating runs in a systematic study of process parameters. To delve deeper into the intricacies of ALD dynamics, specifically focusing on processing time and covering the extensive inner surfaces of SRF cavities with Al_2O_3, we conducted a comprehensive numerical simulation using the ANSYS Fluent 19.1 commercial package software. Our computational model was structured around a 1.3 GHz Tesla-shaped SRF cavity and a thin film sample chamber. We leveraged the boundary conditions for process parameters from our prior experimental work,[23] which notably exhibited no degradation in cavity performance after coating. Subsequently, the simulation results underwent thorough experimental validation, creating a symbiotic relationship between the theoretical and empirical investigations. This amalgamation of theoretical modeling and experimental verification aims at providing a nuanced understanding of the ALD process parameters. Such a holistic approach not only refines considerations for optimizing ALD in SRF cavity applications but also extends insights for any intricate, large volume structures in general.

2. MATHEMATICAL MODELING

ALD process modeling involves decoupling and coupling steps. One ALD cycle can be decoupled into several physical and chemical procedures, such as mass transfer (species transport), momentum transport (material flow), convective heat transfer (system heating), as well as chemical reactions (surface species chemisorption).[35,38] Each process is governed by corresponding partial differential equations (PDEs), which can be solved numerically on the defined domain.[36,37] These PDEs are derived using the finite volume method (FVM). The surface reaction kinetics and mechanisms are defined on surface sites to simulate the material deposition process. In order to obtain solutions to the entire numerical ALD process, the system of PDEs must be coupled together by taking interactions between each physical and chemical process into account.[34−38] The ANSYS fluid dynamics, heat transfer, and chemical kinetics equations used during the simulation work can be found in Section 1 of the Supporting Information.

https://doi.org/10.1021/acs.chemmater.3c03173
Chem. Mater. 2024, 36, 2846−2856

2.1. Surface Reaction Mechanisms. Puurunen's theoretical model on ALD proposed two key chemisorption mechanisms: "ligand exchange" and "dissociation and association".[12,17] In ligand exchange, precursor molecules adsorb onto the substrate, exchanging ligands with surface species to achieve a controlled monolayer growth per ALD cycle. Meanwhile, in dissociation and association, precursor molecules undergo surface adsorption, dissociate into fragments, and then recombine to form a stable monolayer.[12,17] These two mechanisms provide insights into how precursor molecules interact with the substrate to build up the desired thin film one atomic layer at a time.

In order to describe the surface reaction mechanisms, the substrate is presumed to be a silicon wafer with an OH-terminated surface species. This is due to the fact that CH_3-terminated Si substrates are kinetically unfavorable to make surface reaction with water.[39]

In the ligand exchange mechanism, OH* of the substrate exchanged with the methyl group of TMA, as shown in eq 1

$$Al(CH_3)_3 + OH^* \rightarrow CH_3^* + Al(CH_3)_2OH \quad (1)$$

In the case of the chemisorption reaction, a hydrogen atom from the hydroxyl sites at the surface is transferred to one of the methyl groups of TMA. This leads to the formation of gaseous CH_4 and an Al−O bond, as illustrated in eq 2.

$$Al(CH_3)_3 + OH^* \rightarrow {}^*O - AlCH_3 + CH_4 \quad (2)$$

DFT calculation has demonstrated that the chemisorption reactions are significantly more kinetically favorable compared to the ligand exchange reactions.[39] Thus, this study focuses on chemisorption reaction mechanisms for investigating the reactions during both TMA and water pulsing steps.

The overall ALD of Al_2O_3 using TMA and water precursors can be expressed as

$$2Al(CH_3)_3\,(g) + 3H_2O\,(g) \rightarrow Al_2O_3\,(s) + 6CH_4\,(g)\uparrow \quad (3)$$

where (g) and (s) represents gas and solid species, respectively. Equation 3 cannot be used in a chemical kinetic model as it does not reflect the sequential nature of the two precursors pulses. A more intricate chemisorption reaction mechanism for ALD of Al_2O_3, illustrating the sequential ALD pulse and reaction steps, can be depicted by the following pair of half reactions; see eqs 4 and 5: highlighting the surface species (s)

TMA pulse

$$2Al(CH_3)_3\,(g) + 3OH^*\,(s) \rightarrow Al(CH_3)_2^*\,(s) + Al(CH_3)^*\,(s) + 3O\,(s) + 3CH_4\,(g) \quad (4)$$

Water Pulse

$$3H_2O + Al(CH_3)^*\,(s) + Al(CH_3)_2^*\,(s) \rightarrow 3OH^*\,(s) + 2Al\,(s) + 3CH_4\,(g) \quad (5)$$

The details for the two half-cycle reactions of eqs 4 and 5 can be found in Section 1.4 of Supporting Information.

In this study, the chemiosorption reactions in eqs 4 and 5 are used to simulate a complete surface reaction. In addition, the following considerations have been made. (1) The starting surface is OH* terminated for both silicon wafer sample coating chamber and Nb cavity inner surfaces. (2) The starting site densities of OH* is the same for the two substrates (sample chamber and cavity inner surfaces). (3) Only surface reactions are taken into consideration and both half cycle TMA pulse and water pulse reactions are irreversible presuming generation of methane gas.

3. NUMERICAL MODELING

A transient three-dimensional (3D) digital twin is generated mirroring the setup of a homemade[23] ALD system. The model is simulated within the ANSYS Fluent framework. Figure: 1 illustrates the computational domain utilized in the simulation. The setup consists of two precursor containers (for TMA and H_2O) connected to the reaction chamber with a tube. The schematic also displays the precursor inlet and exhaust lines. On the top of the chamber, a schematic of a 1.3 GHz single-cell Tesla-shaped niobium cavity with an inner surface area of about 0.11 m^2 is placed, and its inner volume is considered as an extended reaction chamber. The cavity has a height of 392 mm and inner diameters of 78 mm at the beam tubes and 206 mm at the cell.[40] These values are taken as its boundary condition during the simulation process. The schematics of the thin film chamber can be found in the Figure S1 of the Supporting Information.

In our previous experimental work,[23] the ALD chamber's base pressure was maintained at 10^{-1} Pa through continuous operation of a vacuum pump. Nitrogen gas was utilized as a carrier and purge gas, set at a volumetric flow rate of 20 sccm. The continuous flow of this gas into the reactor volume led to an increase of the working base pressure to approximately ≈100 Pa. The TMA and water precursors were stored in cylindrical containers at room temperature and introduced into the reaction chamber via their inherent vapor pressure. Their specific values, adopted for the numerical model, are 1257.23 and 3157.07 Pa at 25 °C for TMA and water, respectively.[35]

The connection tubing between the precursors and the reaction chamber is always heated to a temperature of 75 °C to avoid condensation of the precursors. The reaction chamber surface is heated to 120 °C. The outlet (stop valve) is connected to the vacuum pump. A pressure boundary is implemented to equate the system's base pressure, established with a nitrogen gas inlet at 100 kPa and a flow rate of 20 sccm. This boundary is set to simulate the operational pressure at the outlet, representing the vacuum pump's full load conditions, approximately at 100 Pa. This configuration assumes a steady flow of N_2 within the system.

During the ALD process, materials are deposited onto the entire inner surface of the ALD system encompassing the whole volume of the cavity, tubing of inlet, and to the exhaust. However, for the purpose of computational efficiency in the numerical model, deposition reactions are exclusively activated on the inner walls of the cavity surface. The temperature is maintained at a constant value of 120 °C, which is the deposition temperature applied during the actual coating. This temperature is selected based on the experimental work reports accounting both the quality of Al_2O_3 deposited[12,23,41] and optimized thermal budget of the cavity.[23] Cavities which are baked under vacuum conditions for long hours at 120−300 °C can alter their performance significantly due to the dissolution of the native oxide layers and various diffusion processes.[28−33] Hence, implementing low temperature coating with minimal annealing impact is desirable[23] to avoid unintentional and nonreproducible changes. The boundary conditions for the other inner walls of the reactor are set to a state of no-slip,

https://doi.org/10.1021/acs.chemmater.3c03173
Chem. Mater. 2024, 36, 2846−2856

ensuring no flux of mass. Meanwhile, these walls' temperature is also fixed at 120 °C (Figure 1).

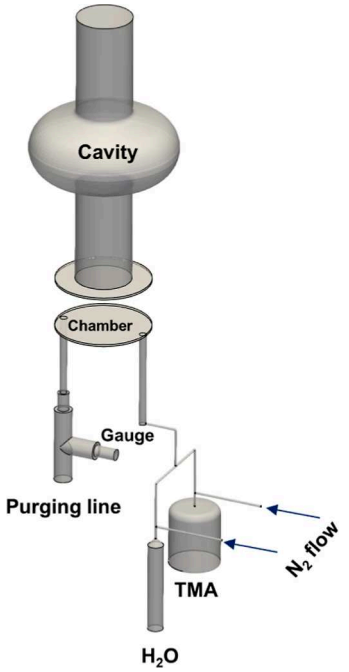

Figure 1. 3D computational domain in the digital twin which is based on the used homemade ALD setup. The system consists of two precursors (TMA and H_2O) inlets and one outlet for exhaust. Reaction chamber for thin film samples and cavity on the top of the chamber: here, the whole cavity is considered as a reaction chamber.

The numerical model is employed to scrutinize an entire cycle of precursor pulsing, exposure, and purging, with the goal of extracting insights concerning both the flow field dynamics and the distribution of gaseous species. Additionally, the mechanisms governing surface reactions, as outlined in eqs 4 and 5 are activated exclusively on the cavity wall and the surface of the sample chamber's bottom wall. This selective activation is aimed at comprehensively investigating the intricacies of the surface deposition process. A flowchart of one full cycle of Al_2O_3 deposition employed in the numerical model for calculating the precursor distribution is depicted in Figure 2. The process boundary conditions for the simulation domain are as follows: First, TMA is pulsed for 50 ms followed by an exposure step for 12 s at which the TMA is chemisorbed by the reaction surface of the cavity wall. Finally, purging for 40 s with the help of nitrogen leads to the removal of excess material and completion of the half cycle. The next half cycle starts with a H_2O pulse for 50 ms and 12 s of exposure with a final purging for 60 s with the help of nitrogen purging gas. These process boundary conditions are adopted from our earlier experimental work,[23] where the recipe was optimized specifically for thin film samples chamber. These conditions are summarized in Table 1.

The numerical simulation is executed within a 3D domain, as illustrated in Figure 3a. The domain is discretized using a nonstructural meshing approach, facilitated by the ANSYS Fluent commercial solver package. Spatial discretization and the estimation of variables such as continuity, energy, and species transport are carried out using a second-order upwind method. The computational values at each node within the domain are determined through a pressure−velocity coupled scheme using the FVM. In terms of time discretization, a second-order implicit method is employed. The adoption of second-order numerical techniques throughout the simulation is a deliberate choice aimed at ensuring a high level of computational accuracy.

4. RESULTS AND DISCUSSION

In this section, we present our simulation results of the precursor distribution and reaction chemistry simulation within the inner volume on the surface of a 1.3 GHz Tesla-shaped SRF cavity. The simulation results of the thin film sample chamber can be found in the Section 3 of the Supporting Information. Furthermore, we present experimental validation to corroborate and complement these simulation findings.

The reaction conditions outlined in Section 2, which are defined by macrolevel parameters such as process temperature, process time, and gas flow rate, serve as the basis for establishing the boundary conditions. The boundary conditions for the processing temperature, the flow rate of N_2 gas, and the pulse, exposure, and purge times of the two precursors are fixed and summarized in Table 1. The starting OH* surface sites density is fixed to 5 sites per nm^2 (8.377×10^9 $kmol/m^2$) for both, sample chamber and niobium cavity, and surfaces according to ref 42.

4.1. Simulation on the Single Cell Cavity Volume.

This part of our study pursued two primary objectives. The first goal aimed at replicating the experiments23 by simulation. To achieve this, having a uniform distribution of precursors across the entire cavity volume by using specified process times and geometries was crucial. This step was integral in validating the accuracy of flow simulations, ensuring consistent and controlled deposition during the ALD process. Subsequently, we aimed at confirming the surface chemistry model's validity

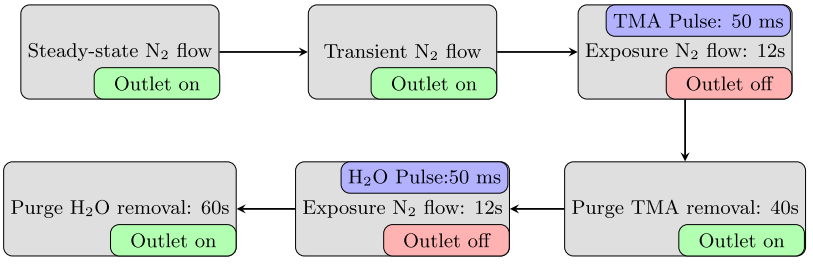

Figure 2. Flowchart for simulating precursors distributions of one full cycle of Al_2O_3 deposition. N_2 is used as a carrier and purging gas. The outlet resembles the stop valve which connects the ALD chamber with the vacuum pump. Outlet is On when the stop valve is open and the chamber is pumped, while outlet is OFF during nonpumping, namely, exposure stage.

https://doi.org/10.1021/acs.chemmater.3c03173
Chem. Mater. 2024, 36, 2846−2856

Table 1. Process Conditions of One Cycle of Al_2O_3 for the Simulation of Precursors Distribution within the Cavity Volume and Thin Film Sample Chamber

TMA			H_2O			temperature	N_2 flow rate
pulse (ms)	exposure (s)	purge (s)	pulse (ms)	exposure (s)	purge (s)	°C	sccm
50	12	40	50	12	60	120	20

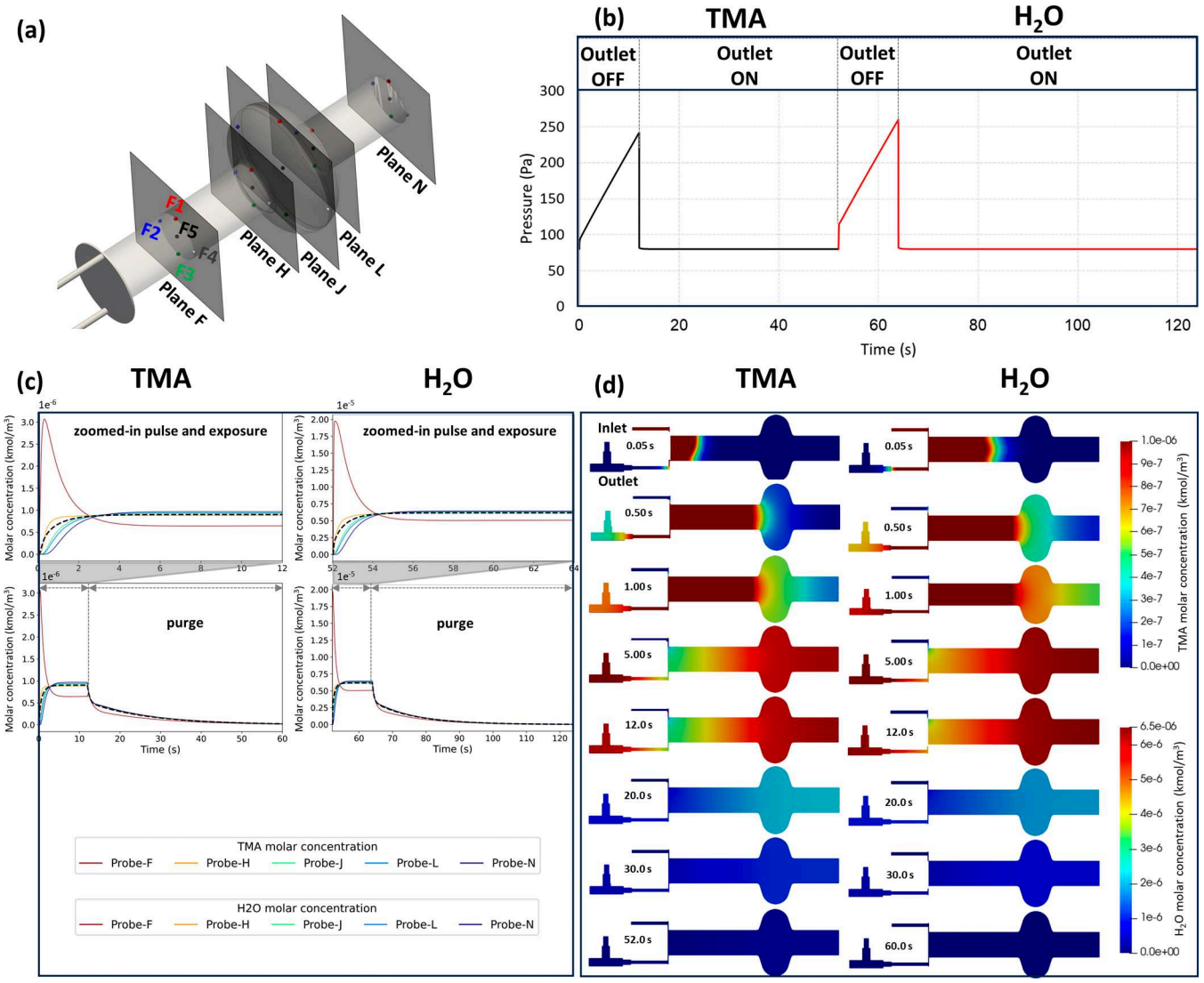

Figure 3. (a) 3D computational domain of a Tesla-shaped 1.3 GHz superconducting cavity. Different planes of F on the bottom tube, H and L on the iris's, J on the equator, and N on the top tube of cavity were used. On each plane five Probe points were assigned to assess the molar concentration of precursors. (b) Pressure vs time for one ALD cycle. The cycle proceeds as follows: a TMA pulse of 50 ms is followed by an exposure time of 12 s; the outlet is off for these steps leading to an increase in pressure. Purging the excess material for 40 s by turning on the outlet leads to a decrease of the pressure and completes the half cycle. The next half cycle starts with a pulse of H_2O for 50 ms with an exposure time of 12 s; outlet is off on these steps and purging for 60 s with outlet on. (c) Left: TMA distribution on the cavity volume during half cycle flow simulation with the inset showing the zoomed pulse and exposure time distribution: The lines serve as guide to the eye. Right: H_2O distribution on the cavity volume during half cycle flow simulation with the inset showing the zoomed pulse and exposure time distribution. The lines serve as guide to the eye: Bottom, legends for TMA and H_2O molar concentration. For both half cycles, an average of probe points are shown for each plane. (d) Contour plots for precursor distribution on the cavity during pulsing, exposure, and purging time of TMA and water precursors.

by determining the deposition rate of Al_2O_3 within the cavity volume. All experimentally observed data were meticulously compared with corresponding simulation predictions.

4.1.1. Precursor Distribution. The numerical study is performed by running two-half cycle simulations. The precursor concentrations are obtained by solving species transport equation with the incorporation of the momentum conservation equation and energy equations (see eqs 2, 4 4 and 6 of Supporting Information).

The schematic representation of the 3D computational domain of a Tesla-shaped 1.3 GHz superconducting cavity used for simulation is shown in Figure 3a. This computational domain is divided into different planes: F and G on the bottom beam tube, M and N on the top beam tube, H and L on the iris's, and I, J, and K on the cell of cavity, which were used. In

https://doi.org/10.1021/acs.chemmater.3c03173
Chem. Mater. 2024, 36, 2846−2856

Figure 3a, only planes F−K are illustrated for clarity (the 3D computational domain with all nine planes can be found in Figure S3 of Supporting Information). Within each of these planes, there are five different probe points assigned; for instance, plane F has F1, F2, F3, F4, and F5. These probe points are located to assess the molar concentration of the precursor gases, and their average values are utilized in this paper. The spatial distribution of probe points allows for a comprehensive evaluation of the precursor distribution and concentration within the cavity volume, enabling a detailed analysis of the ALD process's dynamics and behavior within the structure.

The simulated pressure profile of a complete full cycle of ALD within a cavity volume is illustrated in Figure 3b. The pressure profile is obtained at the outlet. In this profile, the pulse, exposure, and purge times for the two half-cycle processes are consistent with those used in the experiment; see Table 1. Before introducing the precursors, the base pressure of the system is considered as <≈100 Pa, which is the value used during the experimental work.[23]

First, TMA is pulsed into the carrier gas and transported to the cavity, leading to an abrupt pressure increase. This increase corresponds to the rapid introduction of precursor gases into the cavity volume. An exposure time of 12 s leads to a steady increase of the chamber pressure, reaching ≈240 Pa at the end of the exposure time of the first half cycle. This gradual increase indicates that the cavity volume is steadily filled with the purge gas. During this stage of the process, it is presumed that the chemisorption reaction is progressing until saturation is reached. During these two stages of the process, the outlet is OFF, which causes the vacuum pump to be disconnected from the reaction chamber. During the following purging step, the outlet is turned ON for 40 s and a continuous flow of the purging gas N_2 is maintained. During the initial few seconds of the purging step, the pressure rapidly decreased to the initial level of ≈100 Pa and remained constant throughout the entire purging duration.

The second half cycle starts with H_2O pulsing for 50 ms, which also shows an abrupt increase in the pressure. Similar to the first half-cycle, H_2O exposure leads to a steady increase in pressure and reaches ≈260 Pa, and the outlet is OFF during these steps of the process. Here, it is important to mention that the peak pressure values at the end of pulse and exposure times of H_2O are higher compared to those of TMA. This is due to the fact that the vapor pressure of water is higher than that of TMA. H_2O purging for 60 s shows a similar trend as that of TMA, and the pressure value drops to ≈100 Pa. It is important to note that the pressure increases on both half cycles is governed by the following eq 6.

$$PV = (n_{\text{prec.}} + n_{N_2})RT \tag{6}$$

where P is the pressure, V is the volume, R is the ideal gas constant, $n_{\text{prec.}}$ is the amount of the injected precursor molecules, n_{N_2} is the amount of injected nitrogen gas, and T is the temperature.

In eq 6, the amount of injected precursors is fixed, while the amount of injected carrier/purge nitrogen gas is given as a function of process time. It is worth noting that the peak pressure values at the end of the pulse and exposure times during the two-half cycles are lower in the cavity compared to the thin film chamber (Figure S2 of Supporting Information), which can be attributed to the larger volume of the cavity.

In order to calculate the molar concentration of TMA and H_2O in a cavity volume, we discretized the cavity into nine distinct planes, each hosting five probe points (see Figure 3a). The distribution of TMA within the cavity volume during the first half-cycle flow simulation is illustrated on the left in Figure 3c. For a more detailed examination of the distribution dynamics during the pulse and exposure phases, a zoomed-in depiction is presented in Figure 3c. Prior to the introduction of TMA vapor, nitrogen gas is continuously flowed within the cavity volume. Introducing TMA is confirmed by an increase in the molar concentration, which is particularly noticeable at the bottom of the cavity (plane F, red traces). Among the different planes along the cavity, the bottom beam tube planes of F and G exhibit higher TMA concentration than the other planes. Plane F, in particular, shows the highest peak concentration. The concentration profile indicates that as the exposure time progresses, the precursor concentration gradient shifts toward the top of the cavity, probably pushed by the nitrogen. Consequently, during the later stages of exposure time (as seen in the zoomed in inset of Figure 3c), the bottom plane of the cavity shows the lowest concentration compared to other planes. During the purging step, all probe points consistently show a decrease in the molar concentration, reaching almost zero at the end of this phase. The observed decrease in the concentration signifies the effective elimination of excess TMA precursor molecules from the cavity volume during the purging phase. These findings suggest the potential for using a shorter purge time of ≲60 s compared to what was previously reported as the purging time of 120 s in the optimized recipe of a cavity outlined in ref 23.

In the second half of the cycle, the behavior of the H_2O vapor follows a pattern similar to that of TMA, as shown in Figure 3c. Plane F exhibits the highest peak concentration and experiences the earliest dilution among all probe points during the exposure time. During the purging step, a similar trend of continuous molar concentration decrease is observed at all probe points, with saturation occurring at the end of the step. One noticeable difference between the two-half cycles is the peak molar concentration of TMA is lower than that of water, attributed to the lower vapor pressure.

The evolution of the precursor distribution within the cavity volume is effectively visualized through the contour plots of both precursors between the end of the pulse and end of purging time, as shown in Figure 3d. For TMA, at the end of pulsing (50 ms), the vapor concentrated only at the bottom tube of the cavity, and at the end of exposure time (12 s), the top tube of the cavity shows higher concentration. The plots at different purging times effectively illustrate the process of TMA vapor dilution and removal from the cavity volume. H_2O vapor shows similar trends. At the completion of the pulse time, a higher quantity of water vapor is observed within the cavity compared with TMA, a fact confirmed by its elevated vapor pressure. At the end of the exposure time, high concentrations of water vapor are present in the cell and top tube of the cavity, similar to the distribution observed for TMA. Its purging trend closely resembles that of TMA, indicating a potential for a shorter duration compared to the duration reported in ref 23.

In summary, optimizing the process durations for pulsing, exposure, and purging is needed to ensure that the precursor is distributed throughout the cavity. On the other hand, this optimization enables comprehensive coverage of the cavity's intricate geometry and provides minimum times for precursors

https://doi.org/10.1021/acs.chemmater.3c03173
Chem. Mater. 2024, 36, 2846−2856

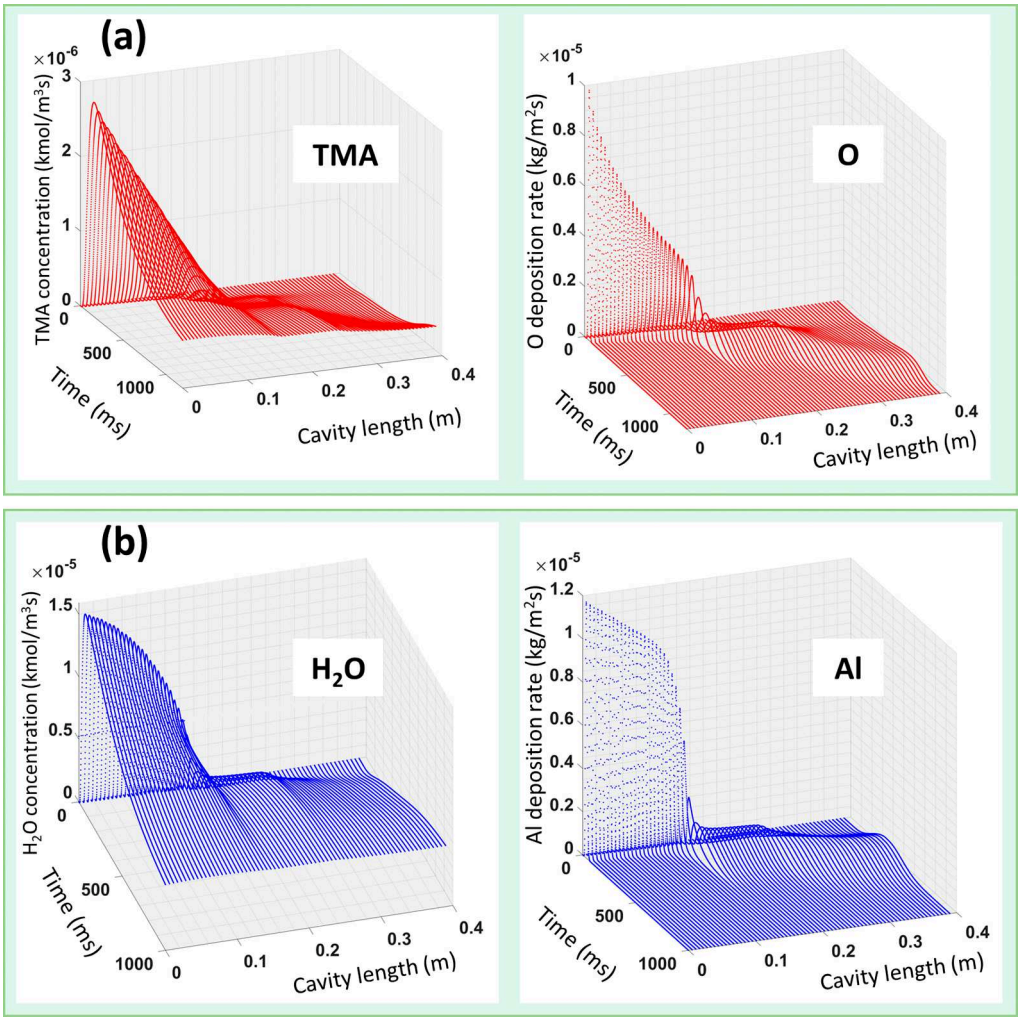

Figure 4. (a) Relation of TMA molar concentration and surface deposition rate of oxygen (O) as a function of a cavity length and time needed for the saturation of the half cycle reaction. Here, the cavity length 0 represents the bottom of the cavity and 0.39 m represents the top of the cavity (b) relation of H_2O molar concentration and the surface deposition rate of aluminum (Al) vs cavity length and time.

to chemisorb onto surfaces, fostering uniform thin film growth, at minimal process times.

4.1.2. Surface Chemistry Simulation. To conduct a more comprehensive investigation into the intricate details of surface reactions, the kinetics of ALD surface chemistry are incorporated into the numerical model (see eqs 9 and 13 of Supporting Information). This integration involves evaluating the production or destruction rate of species (eq 4 of Supporting Information), within the context of species transport and flow simulations. By doing so, we gained a broad understanding of the overall ALD process.

In the surface chemistry simulation, we maintain the same boundary conditions as those utilized for precursor distribution, with the only difference being the process time. Here, we keep the pulse time for both precursors fixed at 50 ms and run the simulation until both half cycles are saturated. This way, the minimum time needed for exposure of both precursors within the cavity volume can be extracted.

The correlations between TMA molar concentration and surface deposition rate of oxygen (O) within the cavity volume as a function of saturation time are depicted in Figure 4a. Initially, the TMA concentration is notably high, particularly at the cavity's bottom area. Over time, this concentration gradually diminishes and spreads across the cavity volume. Approximately at 1.2 s into the process (as depicted in the left plot of Figure 4a), TMA fully distributed throughout the entire cavity volume, maintaining a nonzero concentration. The first half cycle reaches completion as TMA transforms into $Al(CH_3)_2$ and $AlCH_3$, as detailed in reaction eqs 15 and 17 within the Supporting Information. This transformation results in the anchoring of the O and Al atoms on the cavity surface. The reaction reaches saturation at approximately 1 s, evidenced by the oxygen deposition rate declining to 0 at the top of the cavity, as depicted in the right plot of Figure 4a. Note, at this stage of the process, the TMA concentration remains nonzero. This indicates the necessity for an additional purging step before initiating the subsequent half cycle reaction. This necessity is also evident from the contour plots illustrated in Figure 3d.

The relation between the H_2O molar concentration and the surface deposition rate of aluminum (Al) as a function of cavity length and processing time is shown in Figure 4b. Similar to TMA, the pulse duration remains at 50 ms. In this scenario, the two intermediate species, $AlCH_3$ and $Al(CH_3)_2$, react with water (the reaction equations for these intermediate species can be found in the eqs 22 and 23 within the Supporting Information). The reaction reaches saturation at approximately

https://doi.org/10.1021/acs.chemmater.3c03173
Chem. Mater. 2024, 36, 2846−2856

Table 2. R0: the Optimized Recipe Used to Coat SRF Cavities at a Temperature of 120 °C and a N_2 Flow of 20 sccm According to ref 23[a]

	TMA			H_2O			cycles
	pulse/ms	exposure/s	purge/s	pulse/ms	exposure/s	purge/s	
R0—	500	60	120	500	60	120	84
R1—	500	30	120	50	30	120	84
R2—	500	1	120	50	1	120	84
R3—	500	1	90	50	1	90	84
R4—	500	1	60	500	1	60	84
R5—	500	60	30	500	60	30	84
R6—	50	1	120	50	1	120	84
R7—	50	1	90	50	1	90	84
R8—	50	1	60	50	1	60	84

[a]R8: The process times obtained from the precursors distribution and chemical reaction simulation of this work. The total cycle time for R0 and R8 are 361 and 122.1 s, respectively. This demonstrates that the cycle time of R0 is three times longer than that of R8. The validity of R8 is further tested by changing the process times using recipes R1 to R7.

≈750 ms. As observed with TMA, at this stage, the H_2O molar concentration remains nonzero, indicating the necessity for further purging to eliminate excess of H_2O molecules.

Following the pulsing of precursors, TMA reached saturation within ≈1.05 s, while H_2O took only ≈750 ms to reach saturation. At these points in time, some precursors were still distributed within the cavity volume and required purging until their concentrations diminished to zero. These results confirm that having 1 s of exposure time is sufficient to get sufficient precursor at the cavity top for the reaction to happen. This means that having a molar concentration of $(3-4) \times 10^{-7}$is sufficient according to Figure 3d. Figure 4d. In the hypothetical optimal case, one may reduce the pulse time, so all the precursors are consumed and no additional purging is needed.

The calculated thickness of an Al_2O_3 layer for a single full ALD cycle, as simulated within a cavity volume, is determined to be ≈1.22 Å. This value aligns well with the typical GPC of the ALD process.[12,41,43,44] Further details on the calculation methodology can be found in Section 3 of Supporting Information.

Even though the simulated results offer valuable insights into understanding and predicting the physical processes of ALD, interpreting these outcomes requires careful consideration. Idealized assumptions regarding factors such as reaction kinetics, fixed surface site density, consistent sticking probabilities of TMA and H_2O precursors across different process stages, and the absence of impurities may deviate from real experimental conditions.45 Real experiments operate within a complex environment influenced by temperature fluctuations, pressure variations, and the presence of impurities, which can significantly impact outcomes. Replicating these intricacies in simulations proves to be challenging. Additionally, when comparing experimental work with numerical simulations, it is crucial to account for factors like precursor quality and potential measurement errors.

Given these complexities, experimentally examining simulation results becomes imperative. This combined approach—integrating simulated predictions with empirical validation—helps reconcile idealized modeling with real-world complexities, enhancing the robustness and applicability of the findings.

4.2. Experimental Verification. In our previous experimental study,23 we utilized recipe R0, as outlined in Table 2, to achieve a uniformly coated Al_2O_3 layer throughout the cavity volume. However, our simulation results suggested a significant reduction in the process time while preserving film uniformity. To verify these simulations, we conducted an experiment based on the simulation given pulse and exposure times of 50 ms and 1 s, respectively. The latter was chosen as the time both precursors reach saturation, as shown in Figure 4. This experiment also incorporated a 60 s purging duration, derived from the purging time indicated in Figure 3d, serving as the processing time. These parameters collectively define recipe R8, as summarized in Table 2. It is important to note that based on previous simulations, the cycle time has been observed to be three times less compared to the initially experimentally derived value. Consequently, the thermal budget required for depositing the same thickness using an ideal ALD process is approximately three times reduced. In simpler terms, within the same thermal budget, it is now possible to deposit a film three times thicker than previously possible.

The coating procedure employs a dedicated sample holder tailored to match the cavity's contours. This holder accommodates nine Si wafer substrates with a size of 2 × 2 cm^2, arranged and fixed onto the dummy cavity, as illustrated in Figure 5a. In order to check the reproducibility, two samples were placed and analyzed. The film thicknesses were obtained using spectroscopic ellipsometry by taking 12−16 measurements for each sample.

Adhering to recipe R8 from Table 2, the coating process operates at 120 °C with a N_2 flow rate of 20 sccm, spanning 84 cycles of the ALD process. The experimentally recorded pressure profile of the two cycles of coating using recipe R8 can be found in Figure S5(b) of Supporting Information. For a comprehensive understanding of the experimental procedures, detailed information is available in ref 23. The resultant coating with R8 produces a homogeneous layer measuring (10.2 ± 0.5) nm along the cavity surface, as depicted in Figure 5b, affirming the exceptional conformality achieved via the ALD process. The GPC of recipe R8 stands at approximately 1.2 Å, aligning with the calculated GPC showcased in Figure S4 of Supporting Information.

To further test the validity of simulation results, additional experiments were conducted, involving alterations in the processing times of recipes R0 and R8, as detailed in Table 2. Recipes R1−R6 were formulated by adjusting the exposure and purge times of R0, while Recipes R6 and R7 involved modifications to the purge time of R8. The thickness profiles of these films are illustrated in Figure S6 of the Supporting

https://doi.org/10.1021/acs.chemmater.3c03173
Chem. Mater. 2024, 36, 2846−2856

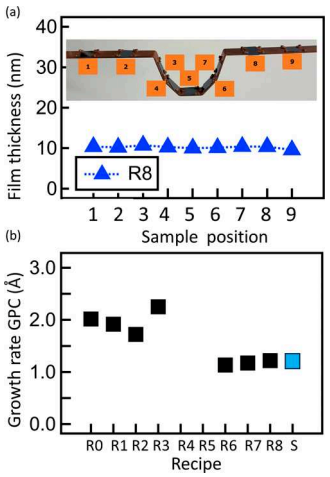

Figure 5. (a) Thickness of the Al_2O_3 layer along the cavity surface for the coating according to the recipe R8 obtained from the simulation work. Sample 9 is at the upmost position, while sample 1 is at the lowest position in the cavity. (b) Growth rate or GPC of different recipes (II) used to further test the validity of the simulation output of recipe R8. The GPC of the simulation result (S) is also plotted (light blues square) for comparison with experimental values.

Information, and the growth rate (GPC) is plotted alongside the simulated GPC in Figure 5b.

For Recipe R0, a reduction solely in the exposure time (as observed in R1 and R2) did not impact the uniformity of the films within the cavity volume but led to a decrease in GPC from 2.1 to 1.8 Å. This reduction in GPC is expected given the shortened time available for further parasitic growth. Conversely, reducing the purging time of R0 by half or more (R4 and R5) resulted in nonuniform growth. Unfortunately, these formulations are unsuitable for cavity coating, as they exhibit characteristics resembling chemical vapor deposition due to inadequate purging between ALD half cycles. On the other hand, within a given short pulse of precursors, increasing the purging time of recipe R8 up to a factor of 2 (as seen in R6 and R7) did not alter the uniformity and GPC of films, as illustrated in Figure S4 of the Supporting Information and Figure 5b. The experimental GPC values for R6, R7, and R8 align well with the simulated GPC, indicating good agreement between experimental and simulated results.

These experimental tests verify the simulation results by showcasing a full coverage, uniform coatings, and the reduction of up to 66.2% of the thermal budget. This reduction presents a dual benefit: First, for Nb SRF cavities, achieving a coating at lower temperatures with a quicker process time is crucial to prevent the diffusion of interstitial oxygen. This diffusion can substantially impact their RF performance, as highlighted in several studies.[28−33] Second, there is an economic advantage in reducing the overall thermal budget, especially for large-volume, complex-shaped ALD coatings conducted on an industrial scale.

5. CONCLUSIONS

This study undertook a systematic exploration, employing both theoretical predictions and experimental verification, to comprehend the precursor flow and surface reaction mechanisms in ALD of Al_2O_3. The 3D computational domain was based on a homemade setup encompassing a 1.3 GHz Tesla-shaped Nb cavity and a thin film sample chamber, utilizing ANSYS Fluent software for simulations. TMA and water were used as precursor materials with varying process times and consistent boundary conditions, such as an initial OH site density at 5/nm^2 and a fixed process temperature of 120 °C.

Initially, precursor distribution simulations for both domains entailed a 50 ms pulse, 12 s exposure for both precursors, and a 40 and 60 s purge for TMA and water, respectively. Subsequently, surface reaction simulations utilized a 50 ms pulse for both precursors, running until both half-cycle reactions reached saturation. Remarkably, TMA saturated at 1.05 s and water at 750 ms. The calculated GPC of Al_2O_3 approximated 1.2 Å, aligning with typical ALD process ranges.

To validate simulation results, additional coatings within the cavity volume were performed by applying the optimized recipe obtained by simulation. The applied recipe then resulted in a uniform Al_2O_3 coverage, and a GPC of 1.2 Å was experimentally observed, perfectly in agreement with the predictions. Additionally, the optimized recipe showcased a potential savings of up to 66.2% in process time, significantly reducing any unwanted impact on cavity performance.

Moreover, this reduction holds economic advantages, particularly for industrial-scale ALD coatings on large and complex structures. This combined approach, integrating simulation predictions with experimental validation, aids in addressing challenges related to harnessing the benefits of ALD for intricate and large-volume structures.

■ ASSOCIATED CONTENT

Supporting Information

The Supporting Information is available free of charge at https://pubs.acs.org/doi/10.1021/acs.chemmater.3c03173.

> Mathematical modeling (ANSYS fluid dynamics equations, heat transfer equations, chemical kinetics equations, and surface reaction mechanism); numerical modeling for the thin film sample chamber; process flow simulation results for the thin film sample chamber; plot of the experimentally recorded pressure profile; and calculated GPC of simulation and plot of thickness of the Al_2O_3 layer along the cavity length coated using recipes R0 to R8 (PDF)

■ AUTHOR INFORMATION

Corresponding Author

Getnet Kacha Deyu − *Institute of Experimental Physics, Universität Hamburg, Hamburg D-22761, Germany;* orcid.org/0000-0001-8760-8155; Email: getnet.kacha.deyu@desy.de

Authors

Trupen Parikh − *Deutsches Elektronen-Synchrotron, Hamburg D-22607, Germany*

Marc Wenskat − *Institute of Experimental Physics, Universität Hamburg, Hamburg D-22761, Germany;* orcid.org/0000-0001-6546-770X

Isabel González Díaz-Palacio − *Institute of Experimental Physics, Universität Hamburg, Hamburg D-22761, Germany; Institute for Nanostructure and Solid State Physics & Center for Hybrid Nanostructures, Universität Hamburg, Hamburg D-22761, Germany*

https://doi.org/10.1021/acs.chemmater.3c03173
Chem. Mater. 2024, 36, 2846−2856

Robert H. Blick − *Institute for Nanostructure and Solid State Physics & Center for Hybrid Nanostructures, Universität Hamburg, Hamburg D-22761, Germany*
Robert Zierold − *Institute for Nanostructure and Solid State Physics & Center for Hybrid Nanostructures, Universität Hamburg, Hamburg D-22761, Germany*
Wolfgang Hillert − *Institute of Experimental Physics, Universität Hamburg, Hamburg D-22761, Germany*

Complete contact information is available at: https://pubs.acs.org/10.1021/acs.chemmater.3c03173

Notes

The authors declare no competing financial interest.

■ ACKNOWLEDGMENTS

This work was supported by the BMBF under the research grants 05H21GURB2 and 05K22GUD.

■ REFERENCES

(1) Padamsee, H. History of gradient advances in SRF. *arXiv* **2020**, 2004.06720 arXiv preprint.
(2) Grassellino, A.; Romanenko, A.; Sergatskov, D.; Melnychuk, O.; Trenikhina, Y.; Crawford, A.; Rowe, A.; Wong, M.; Khabiboulline, T.; Barkov, F. Nitrogen and argon doping of niobium for superconducting radio frequency cavities: a pathway to highly efficient accelerating structures. *Supercond. Sci. Technol.* **2013**, *26* (10), 102001. stacks.iop.org/SUST/26/10200web1
(3) Grassellino, A.; Romanenko, A.; Trenikhina, Y.; Checchin, M.; Martinello, M.; Melnychuk, O. S.; Chandrasekaran, S.; Sergatskov, D. A.; Posen, S.; Crawford, A. C.; et al. Unprecedented quality factors at accelerating gradients up to 45MVm-1 in niobium superconducting resonators via low temperature nitrogen infusion. *Supercond. Sci. Technol.* **2017**, *30*, 094004.
(4) Posen, S.; Romanenko, A.; Grassellino, A.; Melnychuk, O. S.; Sergatskov, D. A. Ultralow surface resistance via vacuum heat treatment of superconducting radio-frequency cavities. *Phys. Rev. Appl.* **2020**, *13*, 014024.
(5) Valente-Feliciano, A.-M. Superconducting RF materials other than bulk niobium: a review. *Supercond. Sci. Technol.* **2016**, *29*, 113002.
(6) Valente-Feliciano, A.-M.; et al. Next-Generation Superconducting RF Technology based on Advanced Thin Film Technologies and Innovative Materials for Accelerator Enhanced Performance and Energy Reach. *arXiv* **2022**, 2204.02536 arXiv preprint.
(7) Díaz-Palacio, Ǵ.; Marc Wenskat, I.; Kacha Deyu, G.; Hillert, W.; Blick, R. H. Robert Zierold "Thermal annealing of superconducting niobium titanium nitride thin films deposited by plasma-enhanced atomic layer deposition. *J. Appl. Phys.* **2023**, *134* (3), 035301.
(8) Gurevich, A. Enhancement of RF breakdown field of superconductors by multilayer coating. *Appl. Phys. Lett.* **2006**, *88*, 012511.
(9) Posen, S.; Transtrum, M. K.; Catelani, G.; Liepe, M. U.; Sethna, J. P. Shielding superconductors with thin films as applied to rf cavities for particle accelerators. *Phys. Rev. Appl.* **2015**, *4*, 044019.
(10) Kubo, T. Superheating fields of semi-infinite superconductors and layered superconductors in the diffusive limit: structural optimization based on the microscopic theory. *Supercond. Sci. Technol.* **2021**, *34*, 045006.
(11) George, S. M. Atomic layer deposition: an overview. *Chem. Rev.* **2010**, *110* (1), 111−131.
(12) Puurunen, R. L. Surface chemistry of atomic layer deposition: A case study for the trimethylaluminum/water process. *J. Appl. Phys.* **2005**, *97* (12), 121301.
(13) Profijt, H. B.; Potts, S. E.; van de Sanden, M. C. M.; Kessels, W. M. M. Plasma-assisted atomic layer deposition: basics, opportunities, and challenges. *J. Vac. Sci. Technol., A* **2011**, *29* (5), 050801.
(14) Cremers, V.; Puurunen, R. L.; Dendooven, J. Conformality in atomic layer deposition: Current status overview of analysis and modelling. *Applied Physics Reviews* **2019**, *6* (2), 021302.
(15) Johnson, R. W.; Hultqvist, A.; Bent, S. F. A brief review of atomic layer deposition: from fundamentals to applications. *Mater. Today* **2014**, *17* (5), 236−246.
(16) Bayer, T. J. M.; Wachau, A.; Fuchs, A.; Deuermeier, J.; Klein, A. Atomic layer deposition of Al2O3 onto Sn-doped In2O3: Absence of self-limited adsorption during initial growth by oxygen diffusion from the substrate and band offset modification by Fermi level pinning in Al2O3. *Chem. Mater.* **2012**, *24* (23), 4503−4510.
(17) Puurunen, R. L. Growth per cycle in atomic layer deposition: A theoretical model. *Chem. Vap. Deposition* **2003**, *9* (5), 249−257.
(18) Groner, M. D.; Elam, J.; Fabreguette, F.; George, S. Electrical characterization of thin Al_2O_3 films grown by atomic layer deposition on silicon and various metal substrates. *Thin Solid Films* **2002**, *413*, 186−197.
(19) Tallarida, M.; Kukli, K.; Michling, M.; Ritala, M.; Leskelä, M.; Schmeisser, D. Substrate reactivity effects in the atomic layer deposition of aluminum oxide from trimethylaluminum on ruthenium. *Chem. Mater.* **2011**, *23*, 3159−3168.
(20) Wilt, J.; Goul, R.; Acharya, J.; Sakidja, R.; Wu, J. Z. In situ atomic layer deposition and electron tunneling characterization of monolayer Al_2O_3 on Fe for magnetic tunnel junctions. *AIP Adv.* **2018**, *8*, 125−218.
(21) Chen, L.; Connell, J. G.; Nie, A.; Huang, Z.; Zavadil, K. R.; Klavetter, K. C.; Yuan, Y.; Sharifi-Asl, S.; Shahbazian-Yassar, R.; Libera, J. A.; et al. Lithium metal protected by atomic layer deposition metal oxide for high performance anodes. *J. Mater. Chem. A* **2017**, *5*, 12297−12309.
(22) Gupta, V.; Adams, M. L.; Sellers, J. A.; Niedzwiecki, N.; Rush, N.; Tuckerman, D. B.; Hamilton, M. C. Atomic Layer Deposited Materials as Barrier Layers for Preservation of Nb Superconductivity in Multilayered Thin-Film Structures. *IEEE Trans. Appl. Supercond.* **2021**, *31*, 1−4.
(23) Wenskat, M.; Deyu, G. K.; González Díaz-Palacio, I.; Blick, R. H.; Zierold, R.; Hillert, W. Successful Al2O3 coating of superconducting niobium cavities with thermal ALD. *Supercond. Sci. Technol.* **2022**, *36*, 015010.
(24) Eremeev, G.; Wu, A. T.; Valente-Feliciano, A. M.; Gu, D. Exploring the effect of Al2O3 ALD coating on a high gradient ILC single-cell cavity. In *Proceedings of IPAC*: Louisiana, USA, 2012. https://accelconf.web.cern.ch/IPAC2012/papers/weppc096.pdwebf.
(25) Proslier, T.; et al. Atomic layer deposition for SRF cavities. In *23rd Particle Accelerator Conference PAC09*: Vancouver, Canada, 2009. https://accelconf.web.cern.ch/pac2009/papers/tu5pfp002.pdwebf.
(26) Bira, S.; et al. Progresses on thin film deposition by ALD at IRFU/IJCLab. In *Tesla Technology Collaboration Workshop TTC21*: Hamburg, Germany, 2021. https://indico.desy.de/event/27572/contributions/94312web/.
(27) Proslier, T.; et al. Results from Point Contact Tunnelling Spectroscopy and Atomic Layer Deposition. In *14th International Conference on RF Superconductivity SRF2009*: Berlin, Germany, 2009. https://accelconf.web.cern.ch/SRF2009/talks/tuobau04_talk.pdwebf.
(28) Ciovati, G.; et al. Review of High Field Q-Slope, Cavity Measurements. In *13th International Conference on RF Superconductivity SRF2007*: Beijing, China, 2007. https://accelconf.web.cern.ch/srf2007/PAPERS/TU102.pdwebf.
(29) Ciovati, G.; Myneni, G.; Stevie, F.; Maheshwari, P.; Griffis, D. High field Q slope and the baking effect: Review of recent experimental results and new data on Nb heat treatments. *Phys. Rev. Spec. Top. Accel. Beams* **2010**, *13*, 022002.
(30) Semione, G. D. L.; Pandey, A. D.; Tober, S.; Pfrommer, J.; Poulain, A.; Drnec, J.; Schütz, G.; Keller, T.; Noei, H.; Vonk, V.; et al. Niobium near-surface composition during nitrogen infusion relevant for superconducting radio-frequency cavities. *Phys. Rev. Spec. Top. Accel. Beams* **2019**, *22*, 103102.

(31) Posen, S.; Romanenko, A.; Grassellino, A.; Melnychuk, O.; Sergatskov, D. Ultralow Surface Resistance via Vacuum Heat Treatment of Superconducting Radio-Frequency Cavities. *Phys. Rev. Appl.* **2020**, *13*, 014024.
(32) Wenskat, M.; Čižek, J.; Liedke, M. O.; Butterling, M.; Bate, C.; Haušild, P.; Hirschmann, E.; Wagner, A.; Weise, H. Vacancy-Hydrogen Interaction in Niobium during Low-Temperature Baking. *Sci. Rep.* **2020**, *10* (1), 8300.
(33) Bafia, D.; et al. The Role of Oxygen Concentration in Enabling High Gradients in Niobium SRF Cavities. In *20th International Conference on RF Superconductivity SRF21, THPTEV016, East Lansing*: USA, 2021. https://lss.fnal.gov/archive/2021/conf/fermilab-conf-21-320-td.pdwebf.
(34) Pan, D.; Guan, D.; Jen, T. C.; Yuan, C. Atomic layer deposition process modeling and experimental investigation for sustainable manufacturing of nano thin films. *J. Manuf. Sci. Eng.* **2016**, *138*, 138.10.
(35) Pan, D.; Ma, L.; Xie, Y.; Jen, T. C.; Yuan, C. On the physical and chemical details of alumina atomic layer deposition: A combined experimental and numerical approach. *J. Vac. Sci. Technol., A* **2015**, *33*, 332.
(36) Pan, D.; Li, T.; Chien Jen, T.; Yuan, C. Numerical modeling of carrier gas flow in atomic layer deposition vacuum reactor: A comparative study of lattice Boltzmann models. *J. Vac. Sci. Technol., A* **2014**, *32*, 32.1.
(37) Pan, D.; Ma, L.; Xie, Y.; Wang, F.; Jen, T. C.; Yuan, C. Experimental and numerical investigations into the transient multi-wafer batch atomic layer deposition process with vertical and horizontal wafer arrangements. *Int. J. Heat Mass Transfer* **2015**, *91*, 416−427.
(38) Pan, D. *Numerical and Experimental Studies of Atomic Layer Deposition for Sustainability Improvement*; The University of Wisconsin-Milwaukee, 2016.(
(39) Delabie, A.; Sioncke, S.; Rip, J.; Van Elshocht, S.; Pourtois, G.; Mueller, M.; Beckhoff, B.; Pierloot, K. Reaction mechanisms for atomic layer deposition of aluminum oxide on semiconductor substrates. *J. Vac. Sci. Technol. A* **2012**, *30*, 01A127.
(40) Aune, B.; Bandelmann, R.; Bloess, D.; Bonin, B.; Bosotti, A.; Champion, M.; Crawford, C.; Deppe, G.; Dwersteg, B.; Edwards, D. A.; et al. Superconducting TESLA cavities. *Phys. Rev. Spec. Top. Accel. Beams* **2000**, *3* (9), 092001.
(41) Kim, S.; Lee, S. H.; Jo, I. H.; Seo, J.; Yoo, Y. E.; Kim, J. H. Influence of growth temperature on dielectric strength of Al_2O_3 thin films prepared via atomic layer deposition at low temperature. *Sci. Rep.* **2022**, *12* (1), 5124.
(42) Gakis, G. P.; Vergnes, H.; Scheid, E.; Vahlas, C.; Boudouvis, A. G.; Caussat, B. Detailed investigation of the surface mechanisms and their interplay with transport phenomena in alumina atomic layer deposition from TMA and water. *Eng. Sci.* **2019**, *195*, 399−412.
(43) Vandalon, V.; Kessels, W. M. M. What is limiting low-temperature atomic layer deposition of Al2O3? A vibrational sum-frequency generation study. *Appl. Phys. Lett.* **2016**, *108* (1), 011607.
(44) Deyu, G. K.; et al. Electrical Properties of Low-Temperature Processed Sn-Doped In_2O_3 Thin Films: The Role of Microstructure and Oxygen Content and the Potential of Defect Modulation Doping. *Materials* **2019**, *12* (14), 2232.
(45) Vandalon, V.; Kessels, W. M. M. E. Initial Growth Study of Atomic-Layer Deposition of Al_2O_3 by Vibrational Sum-Frequency Generation. *Langmuir* **2019**, *35*, 10374−10382.

https://doi.org/10.1021/acs.chemmater.3c03173
Chem. Mater. 2024, 36, 2846−2856